Small molecule donors with different conjugated π linking bridges: Synthesis and photovoltaic properties

Xiyue Dong[1, 2], Dingqin Hu[1], Pengyu Chen[3], Xuexin Dai[4], Chao Hu[1], Zeyun Xiao[1, †], and Shirong Lu[1, †]

[1]Organic Semiconductor Research Center, Chongqing Institute of Green and Intelligent Technology, Chongqing School, University of Chinese Academy of Sciences (UCAS Chongqing), Chinese Academy of Sciences, Chongqing 400714, China

[2]University of Chinese Academy of Sciences, Beijing 100049, China

[3]University of Manchester, Manchester M13 9PL, UK

[4]School of Chemistry and Chemical Engineering, Qiannan Normal University for Nationalities, Duyun 558000, China

Abstract: Three small molecule (SM) donors, namely B-T-CN, B-TT-CN and B-DTT-CN, with different π conjugated bridges were synthesized in this research. Interestingly, with the conjugated fused rings of the π linking bridge increasing, the SM HOMO levels exhibit a decline tendency with –5.27 eV for B-T-CN, –5.31 eV for B-TT-CN and –5.40 eV for B-DTT-CN. After blending the SM donors with the fullerene acceptor $PC_{71}BM$, the all SM organic solar cells (OSCs) achieved high V_{ocs} of 0.90 to 0.96 V. However, the phase separation morphology and molecule stacking are also unexpectedly changed together with the enhancement of conjugated degree of π bridges, resulting in a lower power conversion efficiency (PCE) for the B-DTT-CN:$PC_{71}BM$ device. Our results demonstrate and provide a useful way to enhance OSC V_{oc} and the morphology needs to be further optimized.

Key words: organic solar cell; small molecule donor; molecule energy levels; morphology

1. Introduction

Bulk heterojunction (BHJ) solar cells have attracted extensive attention due to their lightweight, flexibility and potential low cost by solution and roll-to-roll print processes[1–4]. As a result of the development of new materials and device engineering, polymer based organic solar cells (OSCs) have achieved over 17% power conversion efficiencies (PCEs) in single-junction BHJ[5, 6]. However, considering the drawbacks of polymers, such as molecular weight uncertainty, polydispersity and batch-to-batch variation, the OSCs are still far from industrialization[7, 8]. Compared with the polymer, small molecule (SM) donors have advantages such as specific molecular weight, an adjustable chemical structure to easily control the molecular absorption and energy levels, and an easy process to purify[9, 10]. Recently, accompanied with the non-fullerene acceptor (NFA) development (e.g., Y6)[11], the PCEs of small molecular OSCs have progressed thanks to the significant improvement of the short-circuit current (J_{sc})[12–16]. Based on the premise of high J_{sc} value, researchers are paying more attention to enhancing open circuit voltage (V_{oc}) to obtain further improvement of PCEs. The construct of small molecular donors traditionally consists of electron donor core, electron deficiency ending group and the π linking bridge (A-π-D-π-A type). As shown in the molecular molding (Fig. S1), the electron donor parts are mostly distributed on

the donor core and π linking bridge while the electron deficient part is located on the acceptor moiety, which determines the molecular energy levels and even the device V_{oc}. Because the conjugated skeleton is limited, the SMs that are usually present insufficient π–π stacking probability and mobility[17, 18]. Many researchers have systematically studied the influence of donor core and ending group on the SM OSCs[19–21]. It should be noted that the π linking bridge also plays an irreplaceable function to adjust molecular aggregation and molecular stacking, and determines molecular energy levels[12, 15, 22].

Herein, we focus on the π bridge engineering and design three small molecular donors consisting of the benzodithiophene (BDT) core, the cyano-ester ending group with branched alkyl chains to improve the solubility[23], and three types of π linking bridge with different fused ring length to explore their influence on molecule and device properties. The SM donors with the alpha-terthiophene, thieno[3,2-b]thiophene-thiophene and dithieno[2,3-b:2',3'-D]thiophene π linking bridges are named B-T-CN, B-TT-CN and B-DTT-CN respectively (Fig. 1). The difference among the donor molecules is only the π bridges, while the V_{oc} value of the primary devices shows a distinct difference, 0.90 V for B-T-CN based, 0.94 V for B-TT-CN based and 0.96 V for B-DTT-CN based devices, respectively. We employed the cyclic voltammetry (CV) to estimate the molecular energy levels and found that the highest occupied molecular orbital (HOMO) energy levels decline as the fused rings of π linking bridge increase, while deeper HOMO levels for the donor afford higher V_{oc} for devices. Moreover, we employed atomic force microscopy
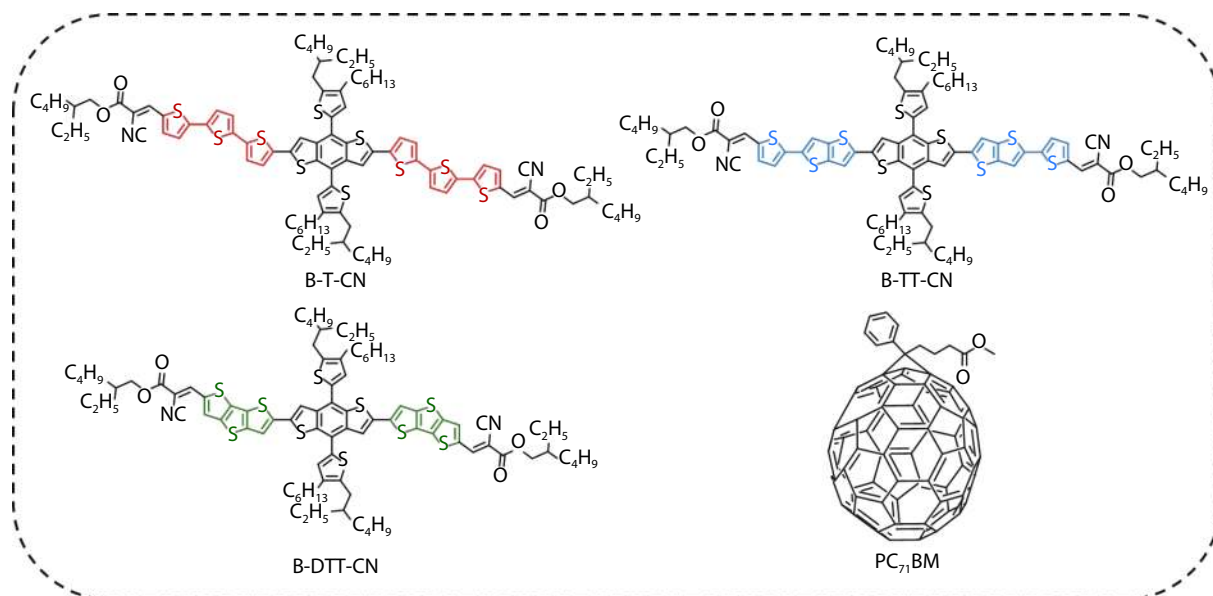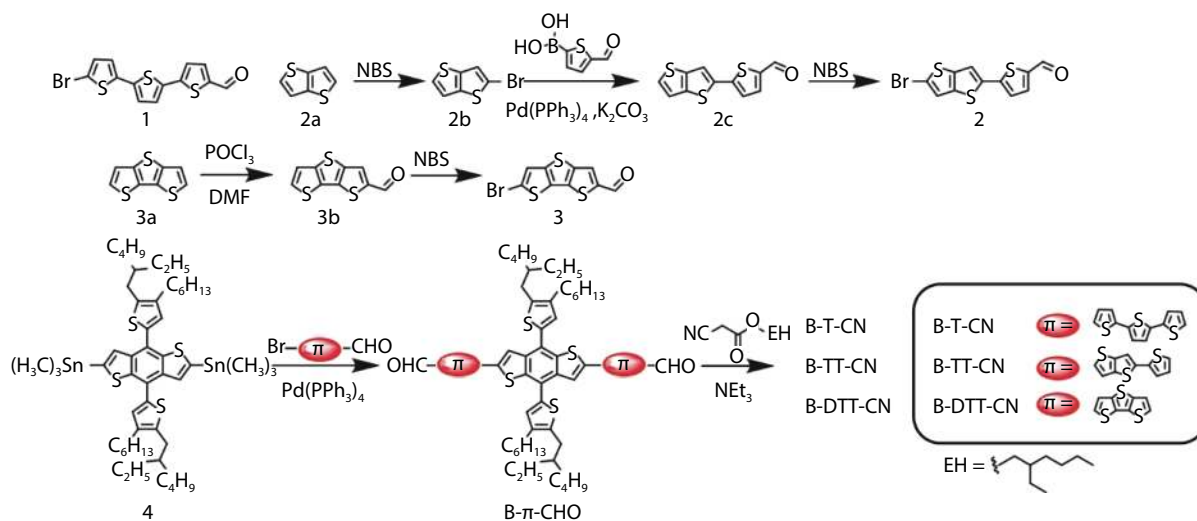
Fig. 1. (Color online) Molecular structures of B-T-CN, B-TT-CN, B-DTT-CN, and PC$_{71}$BM.

Scheme 1. (Color online) Synthetic routes of B-T-CN, B-TT-CN, and B-DTT-CN.

(AFM) and grazing-incidence wide-angle X-ray scattering (GI-WAXS) to explore the influence of three different π bridge-based donors on the blend film morphology and molecular stacking. The B-T-CN:PC$_{71}$BM shows more optimized donor/acceptor interfaces and molecular aggregation for exciton dissociation and transportation and a majority of molecules tend to take a uniform edge-on π–π stacking for efficient intermolecular carrier transport. We systemically design and synthesize three SM donors with different π linking bridges to adjust the material HOMO levels, which provides a new method of molecular design to promote V_{oc} value for high efficiency systems.

2. Results and discussion

2.1. Synthesis and characterizations

The B-T-CN, B-TT-CN and B-DTT-CN were synthesized by n-bromosuccinimide bromination, Vilsmerier-Haack formylation, Suzuki and Stille coupling and Knoevenagel condensation, and the detailed synthetic routes are shown as Scheme 1 and in the Supporting Information. All of the intermediates and final products were fully characterized (Supporting Information). The thermal stabilities of three donors were measured by thermal gravimetric analysis (TGA) and the 5% weight loss decomposition temperatures are 341 °C for B-T-CN, 353 °C for B-TT-CN and 316 °C for B-DTT-CN, respectively (Fig. S2).

2.2. Optical and electrochemical properties

To obtain potential high J_{sc} values, the absorption of materials should cover from visible light to near infrared region[24]. The UV–Vis spectra of B-T-CN, B-TT-CN and B-DTT-CN in chloroform and neat film are shown in Fig. S3 and Fig. 2(a) and the detailed parameters are summarized in Table 1. In the film condition, three molecules exhibit absorption peaks at 561 nm for B-T-CN, 549 nm for B-TT-CN and 541 nm for B-DTT-CN and another shoulder peaks were found at 609, 596, 588 nm, respectively, which indicates the molecules have intensely intermolecular aggregation[25, 26]. Moreover, the film absorption edge of B-T-CN (666 nm) is larger than the other
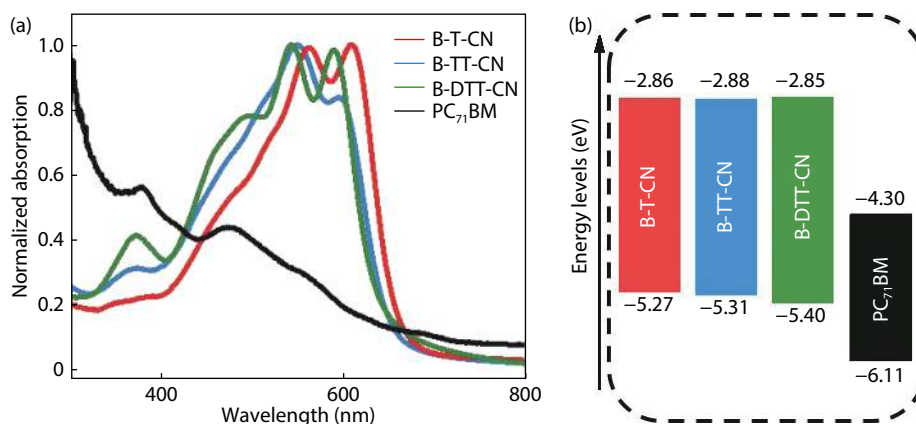
Fig. 2. (Color online) (a) Film absorption of donor and acceptor materials. (b) The energy levels diagram of B-T-CN, B-TT-CN, B-DTT-CN, and PC$_{71}$BM.

Table 1. Optical and electrochemical properties of B-T-CN, B-TT-CN, and B-DTT-CN.

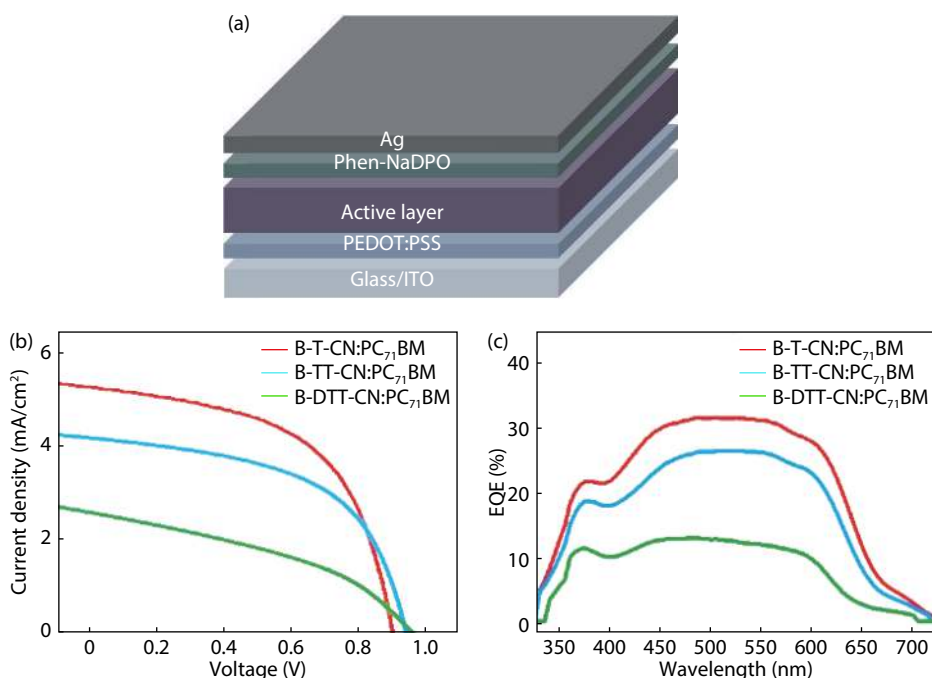| Donor	λ_{peak} (nm)	λ_{onset} (nm)	E_g^{opt} (eV)	E_{HOMO} (eV)	E_{LUMO} (eV)	E_g^{cv} (eV)	T_d (°C)
B-T-CN	561, 609	666	1.86	−5.27	−2.86	2.41	341
B-TT-CN	549, 596	645	1.92	−5.31	−2.88	2.43	353
B-DTT-CN	541, 588	637	1.95	−5.40	−2.85	2.55	316

Fig. 3. (Color online) (a) The device structure of the all small molecule OSCs. (b) Representative current density versus applied voltage curves. (c) EQE spectra of the optimized devices.

two SM donors (645 nm for B-TT-CN, 637 nm for B-DTT-CN) which could generate wider external quantum efficiency (EQE) response[27]. The optical band gaps (E_g^{opt}) of three molecules are estimated by formula as $E_g^{opt} = 1240/\lambda_{onset}$, where the λ_{onset} is the edge of film absorption and defined as 1.86 eV for B-T-CN, 1.92 eV for B-TT-CN, and 1.95 eV for B-DTT-CN, respectively. The molecule HOMO and lowest unoccupied molecular orbital (LUMO) energy levels and electrical band gaps were measured by CV test (Fig. S4), and calculated by formula as HOMO/LUMO = − [$E^{ox/red}$ − E(Fc/Fc$^+$) + 4.8] eV, where $E^{ox/red}$ is the potential from the first oxidation and reduction peak and E(Fc/Fc$^+$) is the half-wave potential of the standard.

As shown in Fig. 2(b), the HOMO levels are slightly deeper as the conjugated fused rings increasing (−5.27 eV for B-T-CN, −5.31 eV for B-TT-CN, and −5.40 for B-DTT-CN) which could lead to higher V_{oc} value in OSCs[28]. The LUMO levels exhibit little difference attributed to the same ending group on the chemical structures and the huge LUMO difference with the acceptor (PC$_{71}$BM) could give sufficient driving force for the carrier separation at the D/A interface[29].

2.3. Photovoltaic performance

To explore the potential photovoltaic properties of three small molecular donors, thin film BHJ SM OSCs were fabri-
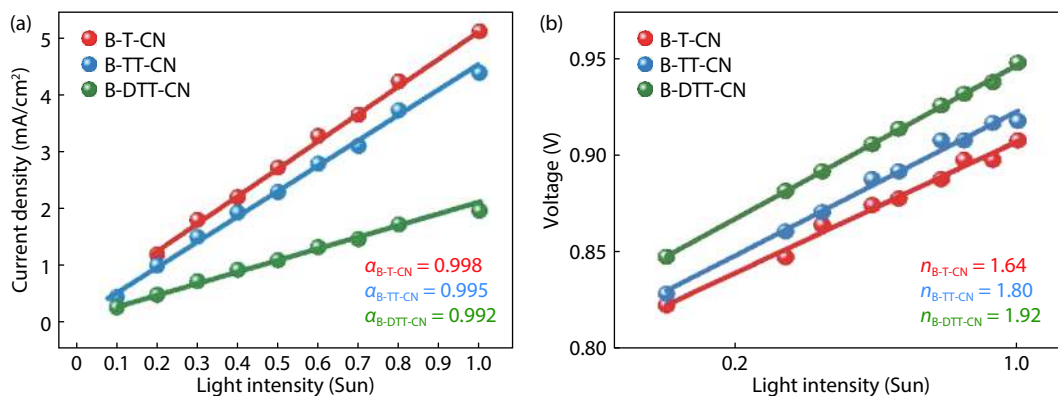
Fig. 4. (Color online) (a) J_{sc} versus light intensity. (b) V_{oc} versus light intensity relationships.

Table 2.   Photovoltaic performances of B-T-CN:PC$_{71}$BM-, B-TT-CN:PC$_{71}$BM-, and B-DTT-CN:PC$_{71}$BM-based OSC devices.

Active layer	V_{oc} (V)	J_{sc} (mA/cm^2)	FF (%)	PCE (%)
B-T-CN:PC$_{71}$BM	0.90	5.29	55.7	2.65
B-TT-CN:PC$_{71}$BM	0.94	4.20	54.8	2.16
B-DTT-CN:PC$_{71}$BM	0.96	2.61	39.8	1.00

cated using a conventional device structure of indium tin oxide (ITO)/poly(3,4-ethylenedioxythiopene):poly(styrene sulfonate) (PEDOT:PSS)/B-T-CN or B-TT-CN or B-DTT-CN:PC$_{71}$BM/Phen-NaDPO/Ag (Fig. 3(a), device area = 0.11 cm^2). Three independent devices were primarily optimized through adjusting spin coating rotational speed and using solvent vapor annealing treatment (SVA). The champion devices of three materials were treated by tetrahydrofuran SVA for 10 s. The merits of B-T-CN:PC$_{71}$BM, B-TT-CN:PC$_{71}$BM, and B-DTT-CN:PC$_{71}$BM based devices parameters are summarized in Table 2 which were tested under simulated AM 1.5G irradiation (100 mW/cm^2) condition. Fig. 3(b) shows the best devices J–V curves. The V_{oc} values of three devices (0.90 V for B-T-CN:PC$_{71}$BM, 0.94 V for B-TT-CN:PC$_{71}$BM, and 0.96 V for B-DTT-CN:PC$_{71}$BM) are gradually increased as the fused ring expands, which demonstrates our strategy of adjusting π linking bridge to control molecular energy levels. In addition, the enhanced device V_{oc} is reliable. The EQE spectra of three devices are shown in Fig. 3(c). The photoresponse range for three molecule-based devices is located from 350 to 670 nm which is in consistency with the film absorption. The B-T-CN:PC$_{71}$BM based curve is higher than others in all EQE response region bring a higher J_{sc} for device (5.29 mA/cm^2 for B-T-CN:PC$_{71}$BM, 4.20 mA/cm^2 for B-TT-CN:PC$_{71}$BM, and 2.61 mA/cm^2 for B-DTT-CN:PC$_{71}$BM). Furthermore, The B-DTT-CN:PC$_{71}$BM based device exhibits a significantly lower fill factor (FF) (39.8%) than others (55.7% for B-T-CN:PC$_{71}$BM and 54.8% for B-TT-CN:PC$_{71}$BM), which could be caused by the vast recombination of these devices[30].

2.4. Charge recombination

Based on the optimal devices, we explored the charge recombination of each material based system to explain the difference of device properties. Firstly, we studied J_{sc} under different incident light intensities to evaluate the degree suffering from bimolecular recombination of devices. As previous studies, the dependence of current density on incident light intens-

ity (I) obey to the power law equation as $J \propto I^{\alpha}$, where α represents the power factor. Briefly, fitting α value is between 0 to 1, the value more closes to 1 means the devices are less influenced by bimolecular recombination[31, 32]. From Fig. 4(a), we found that the α values are 0.998 for B-T-CN:PC$_{71}$BM, 0.995 for B-TT-CN:PC$_{71}$BM, and 0.992 for B-DTT-CN:PC$_{71}$BM based devices respectively which indicate three systems have less bimolecular recombination in the devices. A slightly increased α of B-T-CN:PC$_{71}$BM based devices suggests more efficient charge extraction in devices, which is consistent with the higher FF value. For trap-assistant recombination, we measured V_{oc} under various incident light intensities to estimate it. Similarly, the fitting curves of V_{oc} under different incident light intensities (I) are also complied with another relationship as $V_{oc} \propto nkT/q\ln(I)$, where k is the Boltzmann constant, T is the temperature in Kelvin, and q is the elementary charge. The parameter n represents the degree suffering from trap assistant recombination of devices which is often between at 1 to 2[33, 34]. Generally, the n value more far away from 1 means the devices have more serious carrier traps crossed the active layer or at the interface between the organic semiconductor and the electrode[32, 35]. As the fitted data shown in Fig. 4(b), the n values are 1.64 for B-T-CN:PC$_{71}$BM, 1.80 for B-TT-CN:PC$_{71}$BM, and 1.92 for B-DTT-CN:PC$_{71}$BM based devices, respectively, which indicates that the trap recombination seriously occurred in B-TT-CN:PC$_{71}$BM and B-DTT-CN:PC$_{71}$BM based devices.

Furthermore, we measured the hole and electron carrier mobilities by space charge limited current (SCLC) method (Fig. 5). For hole-only device, the device structure is ITO/MoO$_3$/active layer/MoO$_3$/Ag, and electron-only cell was fabricated with the device architectures as ITO/ZnO/Phen-NaDPO/active layer/Phen-NaDPO/Ag. After blending with PC$_{71}$BM, the B-T-CN:PC$_{71}$BM exhibited both higher hole mobility of 2.55×10^{-5} cm^2/(V·s) and electron mobility of 3.37×10^{-5} cm^2/(V·s) than B-TT-CN:PC$_{71}$BM (hole mobility of 1.25×10^{-5} cm^2/(V·s) and electron mobility of 1.87×10^{-5} cm^2/(V·s)) and B-DTT-CN:PC$_{71}$BM (hole mobility of 9.14×10^{-6} cm^2/(V·s) and electron mobility of 1.58×10^{-5} cm^2/(V·s)). Even though the three small molecule donors have a similar chemical backbone, the blend mobilities are mainly affected by the film morphology which will be discussed in the next section. The ratio of μ_e and μ_h can evaluate the recombination of devices. As the conjugated fused rings of π bridges increase, the devices present a bigger μ_e/μ_h ratio as 1.73 for B-DTT-
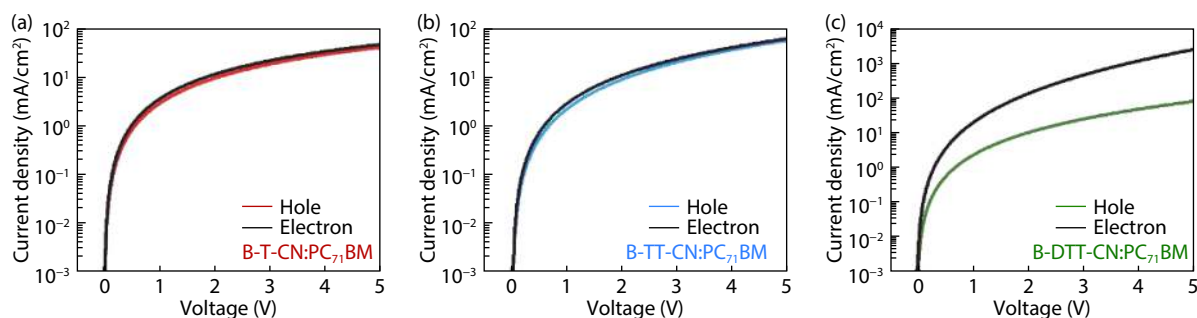
Fig. 5. (Color online) Hole/electron mobility of optimized (a) B-T-CN:PC$_{71}$BM film, (b) B-TT-CN:PC$_{71}$BM film, and (c) B-DTT-CN:PC$_{71}$BM film.
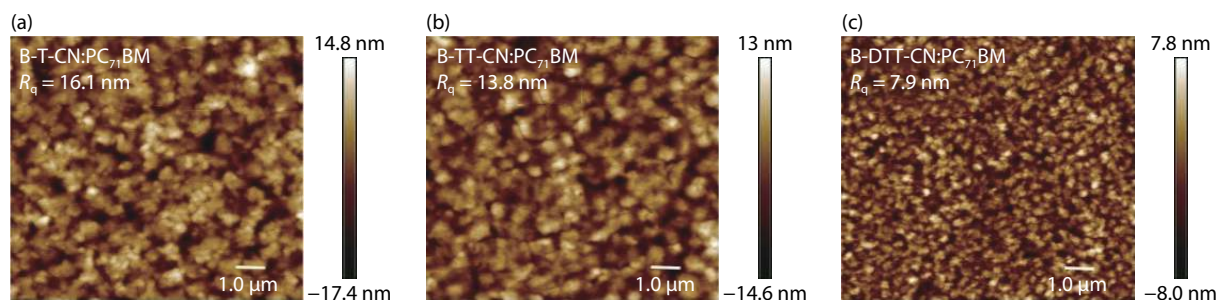

Fig. 6. (Color online) Surface morphology of blend films. AFM height images of (a) B-T-CN:PC$_{71}$BM blend film, (b) B-TT-CN:PC$_{71}$BM blend film, and (c) B-DTT-CN:PC$_{71}$BM blend film.

CN:PC$_{71}$BM, 1.50 for B-TT-CN:PC$_{71}$BM, and 1.32 for B-T-CN:PC$_{71}$BM respectively. The more balanced mobility of B-T-CN:PC$_{71}$BM could bring a lower recombination device, which is consistent with the fill factor result.

2.5. Blend morphology

As mentioned earlier, three devices are mainly affected by trap-assistant recombination. To better understand the charge recombination, we employed AFM and GIWAXS measurements to find the structure–properties relationship, and to analyze the active layers morphology and molecular stacking[36]. Under the same device processing condition, we measured the AFM phase images of active layers (Figs. 6(a)–6(c)). It is clear that the B-T-CN based film (Fig. 6(a)) exhibits an obvious "interpenetrating network" with acceptors and well-defined domain areas, which could produce enough interface and moderate pure donor or acceptor domain for carrier dissociation and transportation. Besides, the root mean square (RMS) roughness of blends is 16.1 nm for B-T-CN:PC$_{71}$BM, 13.8 nm for B-TT-CN:PC$_{71}$BM, and 7.9 nm for B-DTT-CN:PC$_{71}$BM based films, respectively. The higher RMS value of B-T-CN:PC$_{71}$BM based active layer means that the molecules are more likely to form a great crystallization, which could benefit the intermolecular charge transportation[37]. It is known that excellent blend morphology and moderate molecular aggregation are key factors for the less trap recombination. For B-T-CN:PC$_{71}$BM based blend film, more optimized blend morphology to prevent trap generation afforded better device performances than others. The huge morphological difference in the three donor based blends illustrates that the conjugated π linking bridges with different conjugated lengths play a crucial role to adjust molecule aggregation when blended with the same acceptor.

We also employed GIWAXS to study the insight molecular stacking of blend films[38]. In organic materials, the inter-

molecular π–π stacking has two directions as in-plane (IP) and out-of-plane (OOP) which produce diffraction peaks around 1.7 Å^{-1} (010). As shown in Figs. 7(a)–7(c), all of the molecular donors have well-defined edge-on π–π stacking in blend films. Detailed IP and OOP scattering profiles of blend films are shown in Figs. S5(a)–S5(c). Moreover, distribution of azimuthal angle of π–π stacking from 0° to 90° (Fig. 7(d)) proves that the B-T-CN:PC$_{71}$BM and B-TT-CN:PC$_{71}$BM based blends prefer an edge-on orientation for efficient intermolecular charge transport, while the B-DTT-CN:PC$_{71}$BM based blend exhibits isotropy orientation at π–π staking area which could result in abundant recombination[39, 40]. Compared with B-DTT-CN based blend, the uniform edge-on π–π stacking of B-T-CN:PC$_{71}$BM and B-TT-CN:PC$_{71}$BM based blends could provide more charge transport tubes, which is consistent with the devices and recombination results[27, 41].

3. Conclusion

In summary, we have designed and synthesized three different type π linking bridge small molecular donors. By changing conjugated length, the small molecules achieved a deeper HOMO level, which result in a higher V_{oc} for all SM OSCs. The V_{oc} increased from 0.90 V enhance to 0.96 V and an overall PCE of 2.65% for B-T-CN:PC$_{71}$BM based, 2.16% for B-TT-CN:PC$_{71}$BM based and 1.00% for B-DTT-CN:PC$_{71}$BM based devices was achieved. However, the blend morphology and molecular stacking are also changed by adjusting π linking bridges. When the π linking bridge from dithieno[2,3-b:2',3'-D]thiophene (B-DTT-CN) change to alpha-terthiophene (B-T-CN), the blend morphology tends to present more clear interpenetrating network structures and the molecular packing becomes more uniform on the OOP detraction which could provide more moderate D/A interfaces for carrier desolation and more effective intermolecular charge transport tubes to
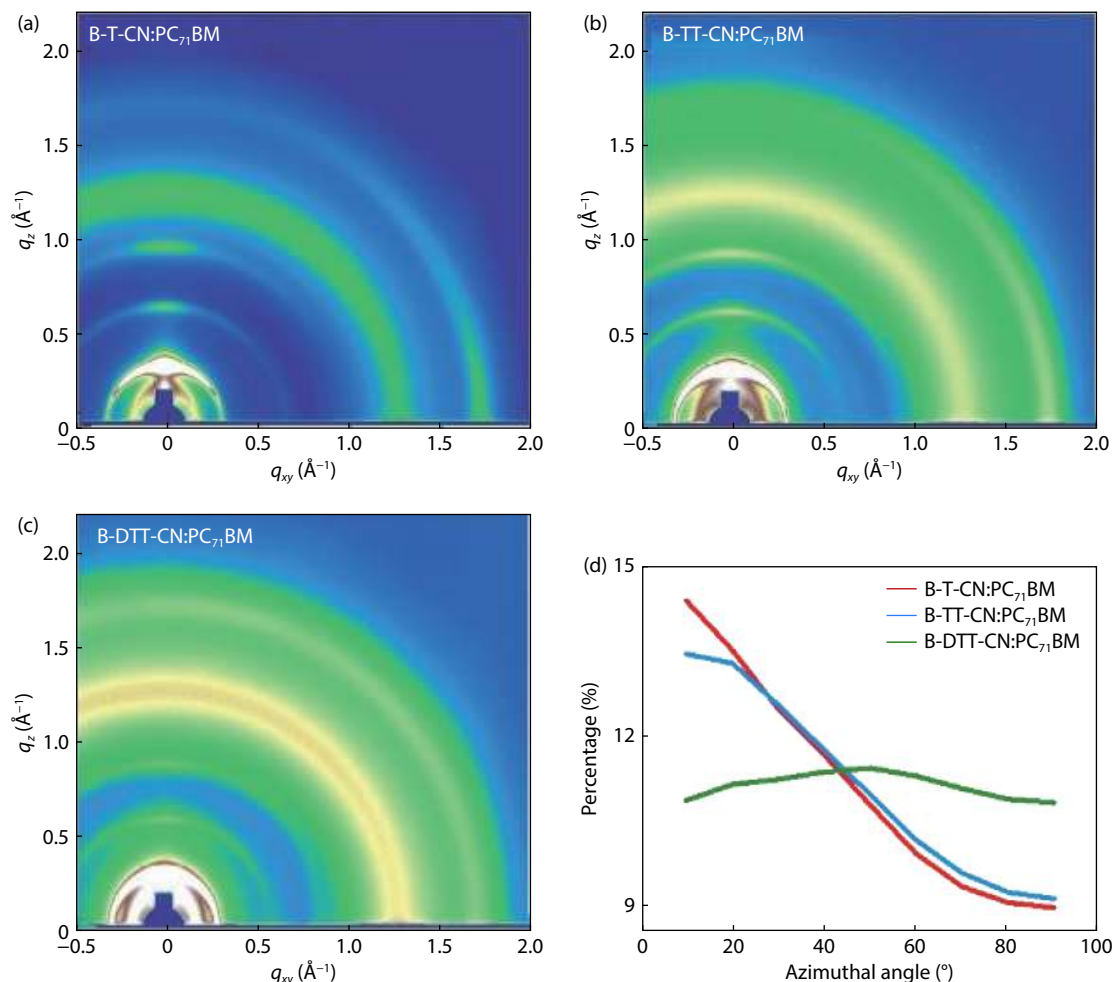
Fig. 7. (Color online) GIWAXS two-dimensional diffraction patterns of (a) B-T-CN:PC$_{71}$BM blend film, (b) B-TT-CN:PC$_{71}$BM blend film, and (c) B-DTT-CN:PC$_{71}$BM blend film. (d)The azimuthal angle distribution of π–π stacking.

ensure less trap recombination and increased J_{sc}. Our research provides a method to enhance OSC V_{oc}, which could promote the development of high efficiency OSCs.

References

[1]   Lu L Y, Zheng T Y, Wu Q H, et al. Recent advances in bulk heterojunction polymer solar cells. Chem Rev, 2015, 115, 12666

[2]   Zhao F W, Dai S X, Wu Y, et al. Single-junction binary-blend nonfullerene polymer solar cells with 12.1% efficiency. Adv Mater, 2017, 29, 1700144

[3]   Lin Y Z, Zhan X W. Oligomer molecules for efficient organic photovoltaics. Acc Chem Res, 2016, 49, 175

[4]   Hou J, Inganäs O, Friend R H, et al. Organic solar cells based on non-fullerene acceptors. Nat Mater, 2018, 17, 119

[5]   Liu Q S, Jiang Y F, Jin K, et al. 18% efficiency organic solar cells. Sci Bull, 2020, 65, 272

[6]   Cui Y, Yao H F, Zhang J Q, et al. Single-junction organic photovoltaic cells with approaching 18% efficiency. Adv Mater, 2020, 32, 1908205

[7]   Chen Y S, Wan X J, Long G K. High performance photovoltaic applications using solution-processed small molecules. Acc Chem Res, 2013, 46, 2645

[8]   Collins S D, Ran N A, Heiber M C, et al. Small is powerful: Recent progress in solution-processed small molecule solar cells. Adv Energy Mater, 2017, 7, 1602242

[9]   Huo Y, Zhang H L, Zhan X W. Nonfullerene all-small-molecule organic solar cells. ACS Energy Lett, 2019, 4, 1241

[10]   Zhou Z C, Xu S J, Song J N, et al. High-efficiency small-molecule ternary solar cells with a hierarchical morphology enabled by synergizing fullerene and non-fullerene acceptors. Nat Energy, 2018, 3, 952

[11]   Yuan J, Zhang Y Q, Zhou L Y, et al. Single-junction organic solar cell with over 15% efficiency using fused-ring acceptor with electron-deficient core. Joule, 2019, 3, 1140

[12]   Dong X Y, Yang K, Tang H, et al. Improving molecular planarity by changing alky chain position enables 12.3% efficiency all-small-molecule organic solar cells with enhanced carrier lifetime and reduced recombination. Sol RRL, 2020, 4, 1900326

[13]   Yue Q H, Wu H, Zhou Z C, et al. 13.7% efficiency small-molecule solar cells enabled by a combination of material and morphology optimization. Adv Mater, 2019, 31, 1904283

[14]   Ge J F, Xie L C, Peng R X, et al. 13.34% efficiency non-fullerene all-small-molecule organic solar cells enabled by modulating the crystallinity of donors via a fluorination strategy. Angew Chem Int Ed, 2020, 59, 2808

[15]   Gao J, Ge J F, Peng R X, et al. Over 14% efficiency nonfullerene all-

small-molecule organic solar cells enabled by improving the ordering of molecular donors via side-chain engineering. J Mater Chem A, 2020, 8, 7405

[16] Chen H Y, Hu D Q, Yang Q G, et al. All-small-molecule organic solar cells with an ordered liquid crystalline donor. Joule, 2019, 3, 3034

[17] Liu Y S, Wan X J, Wang F, et al. High-performance solar cells using a solution-processed small molecule containing benzodithiophene unit. Adv Mater, 2011, 23, 5387

[18] Kan B, Zhang Q, Li M M, et al. Solution-processed organic solar cells based on dialkylthiol-substituted benzodithiophene unit with efficiency near 10%. J Am Chem Soc, 2014, 136, 15529

[19] Zhou J Y, Wan X J, Liu Y S, et al. Small molecules based on benzo[1, 2-b: 4, 5-b']dithiophene unit for high-performance solution-processed organic solar cells. J Am Chem Soc, 2012, 134, 16345

[20] Ni W, Li M M, Wan X J, et al. A high-performance photovoltaic small molecule developed by modifying the chemical structure and optimizing the morphology of the active layer. RSC Adv, 2014, 4, 31977

[21] Shen S L, Jiang P, He C, et al. Solution-processable organic molecule photovoltaic materials with bithienyl-benzodithiophene central unit and indenedione end groups. Chem Mater, 2013, 25, 2274

[22] Sun K, Xiao Z, Lu S, et al. A molecular nematic liquid crystalline material for high-performance organic photovoltaics. Nat Commun, 2015, 6, 6013

[23] Qiu B, Xue L, Yang Y, et al. All-small-molecule nonfullerene organic solar cells with high fill factor and high efficiency over 10%. Chem Mater, 2017, 29, 7543

[24] Bin H J, Yao J, Yang Y K, et al. High-efficiency all-small-molecule organic solar cells based on an organic molecule donor with alkylsilyl-thienyl conjugated side chains. Adv Mater, 2018, 30, 1706361

[25] Wang Y, Liu B, Koh C W, et al. Facile synthesis of polycyclic aromatic hydrocarbon (PAH)-based acceptors with fine-tuned optoelectronic properties: Toward efficient additive-free nonfullerene organic solar cells. Adv Energy Mater, 2019, 9, 1803976

[26] Wan J H, Xu X P, Zhang G J, et al. Highly efficient halogen-free solvent processed small-molecule organic solar cells enabled by material design and device engineering. Energy Environ Sci, 2017, 10, 1739

[27] Deng D, Zhang Y J, Zhang J Q, et al. Fluorination-enabled optimal morphology leads to over 11% efficiency for inverted small-molecule organic solar cells. Nat Commun, 2016, 7, 13740

[28] Duan T N, Babics M, Seitkhan A, et al. F-Substituted oligothiophenes serve as nonfullerene acceptors in polymer solar cells with open-circuit voltages >1 V. J Mater Chem A, 2018, 6, 9368

[29] Liu D X, Kan B, Ke X, et al. Extended conjugation length of nonfullerene acceptors with improved planarity via noncovalent interactions for high-performance organic solar cells. Adv Energy Mater, 2018, 8, 1801618

[30] Xie Q, Liao X F, Chen L, et al. Random copolymerization realized high efficient polymer solar cells with a record fill factor near 80%. Nano Energy, 2019, 61, 228

[31] Proctor C M, Kuik M, Nguyen T Q. Charge carrier recombination in organic solar cells. Prog Polym Sci, 2013, 38, 1941

[32] Cowan S R, Roy A, Heeger A J. Recombination in polymer-fullerene bulk heterojunction solar cells. Phys Rev B, 2010, 82, 245207

[33] Kirchartz T, Deledalle F, Tuladhar P S, et al. On the differences between dark and light ideality factor in polymer: Fullerene solar cells. J Phys Chem Lett, 2013, 4, 2371

[34] Wheeler S, Deledalle F, Tokmoldin N, et al. Influence of surface recombination on charge-carrier kinetics in organic bulk heterojunction solar cells with nickel oxide interlayers. Phys Rev Appl, 2015, 4, 024020

[35] Liang R Z, Babics M, Savikhin V, et al. Carrier transport and recombination in efficient "all-small-molecule" solar cells with the nonfullerene acceptor IDTBR. Adv Energy Mater, 2018, 8, 1800264

[36] Zhao F W, Wang C R, Zhan X W. Morphology control in organic solar cells. Adv Energy Mater, 2018, 8, 1703147

[37] Duan T N, Gao J, Xu T L, et al. Simple organic donors based on halogenated oligothiophenes for all small molecule solar cells with efficiency over 11%. J Mater Chem A, 2020, 8

[38] Yang L Y, Zhang S Q, He C, et al. Modulating molecular orientation enables efficient non-fullerene small-molecule organic solar cells. Chem Mater, 2018, 30, 30

[39] Vohra V, Kawashima K, Kakara T, et al. Efficient inverted polymer solar cells employing favourable molecular orientation. Nat Photonics, 2015, 9, 403

[40] Jung J, Lee W, Lee C, et al. Controlling molecular orientation of naphthalenediimide-based polymer acceptors for high performance all-polymer solar cells. Adv Energy Mater, 2016, 6, 1600504

[41] Chen S S, Cho H J, Lee J, et al. Modulating the molecular packing and nanophase blending via a random terpolymerization strategy toward 11% efficiency nonfullerene polymer solar cells. Adv Energy Mater, 2017, 7, 1701125